Surface-Based vs. Voxel-Based Finite Element Head Models: Comparative Analyses of Strain Responses

Zhou Zhou,[1*] Xiaogai Li,[1] Svein Kleiven[1]

[1] Division of Neuronic Engineering, KTH Royal Institute of Technology, Stockholm, 14152, Sweden.

[*] Corresponding author, Email: zhouz@kth.se

Contact information of other authors:

Xiaogai Li: xiaogai@kth.se

Svein Kleiven: sveink@kth.se

Abstract

Finite element (FE) models of the human head are important injury assessment tools but developing a high-quality, hexahedral-meshed FE head model without compromising geometric accuracy is a challenging task. Important brain features, such as the cortical folds and ventricles, were captured only in a handful of FE head models that were primarily developed from two meshing techniques, i.e., surface-based meshing with conforming elements to capture the interfacial boundaries and voxel-based meshing by converting the segmented voxels into elements with and without meshing smoothing. Despite these advancements, little knowledge existed of how similar the strain responses were between surface- and voxel-based FE head models. To address this, a previously developed surface-based head model with conforming meshes to capture the cortical folds-subarachnoid cerebrospinal fluid and brain-ventricle interfaces was reused, and two voxel-based models with and without mesh smoothing were newly created here. These three models were employed to simulate head impacts. The results showed remarkable similarities in the strain responses between the surface- and the voxel-based models. When calculating commonly used injury metrics, including the percentile strains below the maximum (e.g., 95 percentile strain) and the volume of brain element with the strain over certain thresholds, the responses of the three models were virtually identical. When examining the strain distribution, the three models showed different patterns at the interfacial boundary (e.g., sulci and gyri in the cortex, regions adjacent to the falx and tentorium) with strain differences exceeding 0.1. The mesh smoothing procedure in the voxel-based models marginally reduced the strain discrepancies compared to the surface-based model. This study yielded new quantitative insights into the general similarity in the strain responses between the surface- and voxel-based FE head models and underscored that caution should be exercised when using the strain at the interface to predict injury.

Keywords

Traumatic brain injury, finite element head models, hexahedral mesh techniques, surface- and voxel-based meshing, brain strain

Introduction

Traumatic brain injury (TBI) represents a critical public health problem. Globally, around 69 million people suffer a TBI each year [1]. In Europe, TBI is the leading cause of death in young adults and its incidence is on the rise in the elderly [2]. TBI is considered a 'silent epidemic', as society is largely unrecognized of the magnitude of this problem [3]. In the European Union, about 7.7 million people are living with a TBI-induced disability [4]. The economic cost of TBI is enormous with a yearly cost of around 33 billion Euros at the European level [5] and 400 billion Euros at the global level [6]. To address this TBI-related urgency, advancing fundamental understandings of the brain injury mechanics and thresholds is crucial for the development of more effective prevention strategies.

Finite element (FE) models of the human head are instrumental in providing quantitative insight into how the external impact instigates localized tissue straining and triggers the injury occurrence [7, 8]. Owing to the intricate complexity of the human head, developing an FE head model for TBI investigation is not a trivial task with manifold variables affecting the injury prediction outcome. The model should have sufficient representations of head sub-components (e.g., brain, ventricle) in terms of geometry [9-12] and material [13-16] as well as accurate descriptions of intracranial interfaces (e.g., brain-ventricle and brain-skull interactions) [17-20]. Careful considerations should also be given to the strategy of geometrical discretization (e.g., mesh type, size, and quality) [21-23], element formulation [23, 24], and other numerical choices (e.g., hourglass control [24, 25]). Before its usage of injury assessment, the model needs to be extensively evaluated by injury-relevant experimental data (e.g., brain motion, strain, and strain rate with the impact severity close to the traumatic level) [26-34]. Even for injury assessment itself, one critical challenge is how best to interpret the spatiotemporally detailed, multiform responses yielded by the FE models (e.g., maximum principal strain (MPS) in the whole brain vs. maximum von Mises stress in the corpus callosum (CC)) to achieve the optimal predictability [35-38]. Thanks to the endeavour of the TBI research community over the past decades, modern FE head models are featured with subject-specific geometry [11, 39], hyper-viscoelastic brain material with tension-compression asymmetry and rate dependency [40, 41], and solid and fluid representations of the intracranial components [17, 18]. Encouraging correlations have been reported between the FE-derived mechanical loading at the brain tissue or its microstructures and clinically diagnosed injury in real life (e.g., concussion, parenchymal haemorrhage) [42-45].

Two important features of the human head are the cortical folds (i.e., gyri and sulci) and ventricles, both of which have important biomechanical roles in the brain's vulnerability. For example, by virtually impacting two FE head models with and without sulci, Ho and Kleiven [46] found that high strain level was concentrated to several spots at the depth of the sulci, as was laterally confirmed in another FE study [47]. Such a strain distribution largely overlapped with the site of certain brain pathologies (i.e., cerebral infarcts in diffuse axonal injury [48] and tau pathology in chronic traumatic

encephalopathy [49]). Recently, Zhou, et al. [50, 51] reported the presence of the ventricles, a cerebrospinal fluid (CSF)-filled cavity, exacerbated the strain in the deep brain regions (e.g., ventricular wall, CC, thalamus), providing a possible explanation for the prevalence of periventricular injury in severe TBI patients [52]. Despite their biomechanical prominence, the cortical folds and ventricles were largely simplified in the existing FE head models [40, 41, 53-59], of which the brain was simplified by smearing out the gyri and sulci with a homogeneous layer of subarachnoid CSF, and certain elements were selected to represent the ventricles.

Generating high-quality meshes without compromising geometric and morphologic details is a challenging task. This is especially the case for the brain as the hexahedral element is generally preferred owing to its stability and accuracy in scenarios with large deformation (e.g., TBI modelling) and material incompressibility (e.g., brain and CSF) [24]. Among the handful of pure hexahedral FE head models featuring cortical folds and ventricles, two different meshing techniques were used. The first one was a surface-based meshing, in which outer surfaces of individual components (e.g., pial surface, ventricular surface) were first generated and hexahedral meshes were deployed to fill the domain encased within the inputted surfaces and capture the boundaries between different components [15, 50, 51, 60, 61]. The other prevalently used method was a voxel-based meshing, in which segmented voxels were converted into hexahedral elements [14, 39, 46, 62-68]. Despite the success of both techniques in generating anatomically detailed FE head models, no knowledge existed of how similar the responses were between the surface- and voxel-based models. When limited to the voxel-based model, a meshing smoothing procedure was often implemented to reduce the jaggedness between different parts (e.g., the interface between the brain and CSF) [14, 46, 65-69]. Although the smoothing procedure is known to reduce the mesh quality [70], its influence on brain strain has not been quantified before.

The current study aimed to answer the research question of how close the strain responses were between the surface- and voxel-based FE head models. To this end, a previously developed surface-based head model [60] was reused here with conforming elements to capture the cortical folds-subarachnoid CSF interface and the brain-ventricle interface, and two voxel-based models were newly created by converting voxels as elements with and without mesh smoothing, respectively. These three models were used to simulate head impacts. Strain comparisons were performed to test two hypotheses: 1) The strain responses of surface-based and voxel-based models were comparable, except for the interfacial region; 2) The meshing smoothing procedure marginally mitigated the strain differences between the surface- and voxel-based models.

Methods

Mesh generation

For the surface-based meshing, its implementation was elaborated by Li, et al. [60] early with the delivered FE head model (Fig 1I) reused here. In brief, the ICBM 152 atlas (isotropic resolution: 1 mm^3) [71] was segmented automatically to delineate the brain (with details of gyri and sulci) and CSF (including subarachnoid CSF and ventricles) (Fig 1A). The skull was created by thresholding the atlas and then removing the brain and CSF masks with manual editing. Triangulated profiles of the brain, subarachnoid CSF, ventricle, and skull were extracted from the segmentation (Fig 1B) and further input to the Hexotic software [72] to automatically generate all hexahedral elements (Fig 1C) using an octree-based method [72-74]. The octree-based method recursively split an initial box (i.e., the root octant that was a perfect cube and covered the whole input profiles) into smaller boxes (i.e., descended octants that were often irregular cubes) until the descendant octants could resolve the local geometry. The recursive level was primarily determined by the complexity of the geometry and a level of eight was empirically chosen to capture the anatomical details of the head profiles appropriately. Given the delivered head model with hexahedral meshes that conformed to the cortical folds-subarachnoid CSF-skull interface and brain-ventricle interface (Fig 1C and Fig 1F), this model was referred to as Conf-model hereafter.

For the voxel-based meshing, a head model (referred to as Vxl-model) was newly developed by directly converting each isotropic voxel in the ICBM atlas (Fig 1A) into a cubic hexahedral element (Fig 1D). Elements with their voxel counterparts that have the same segmentation label were assigned to one part (i.e., brain, subarachnoid CSF, ventricle, skull), the same as the approaches used to develop other models [39, 62-64]. Critically, the resultant mesh had stair-stepped interfaces between the brain and CSF, as was partially evidenced by the enlarged view of the brain surface in Fig 1D and the ventricles in Fig 1G.

To alleviate the issue of jagged interfaces, a Laplacian-based, volume-preserving mesh smoothing algorithm [75] was applied to the Vxl-model, thereby creating a new derivative model herein (referred to Vxls-model, Fig 1E). This smoothing algorithm was implemented via an in-house customized script. In brief, it optimized the locations of those nodes at the exterior surface and intracranial interfaces to balance the need of reducing the jaggedness level between different tissues (see the enlarged view of the brain surface in Fig 1E and the ventricles in Fig 1H) and preserving the volume of head components and element quality. The derivative Vxls-model retained the same element and node numbers and mesh topology as the original Vxl-model. Technical details of this smoothing algorithm were initially presented by Boyd and Müller [75] and its application for smoothing voxel-based FE head models was noted in earlier studies [66, 69].

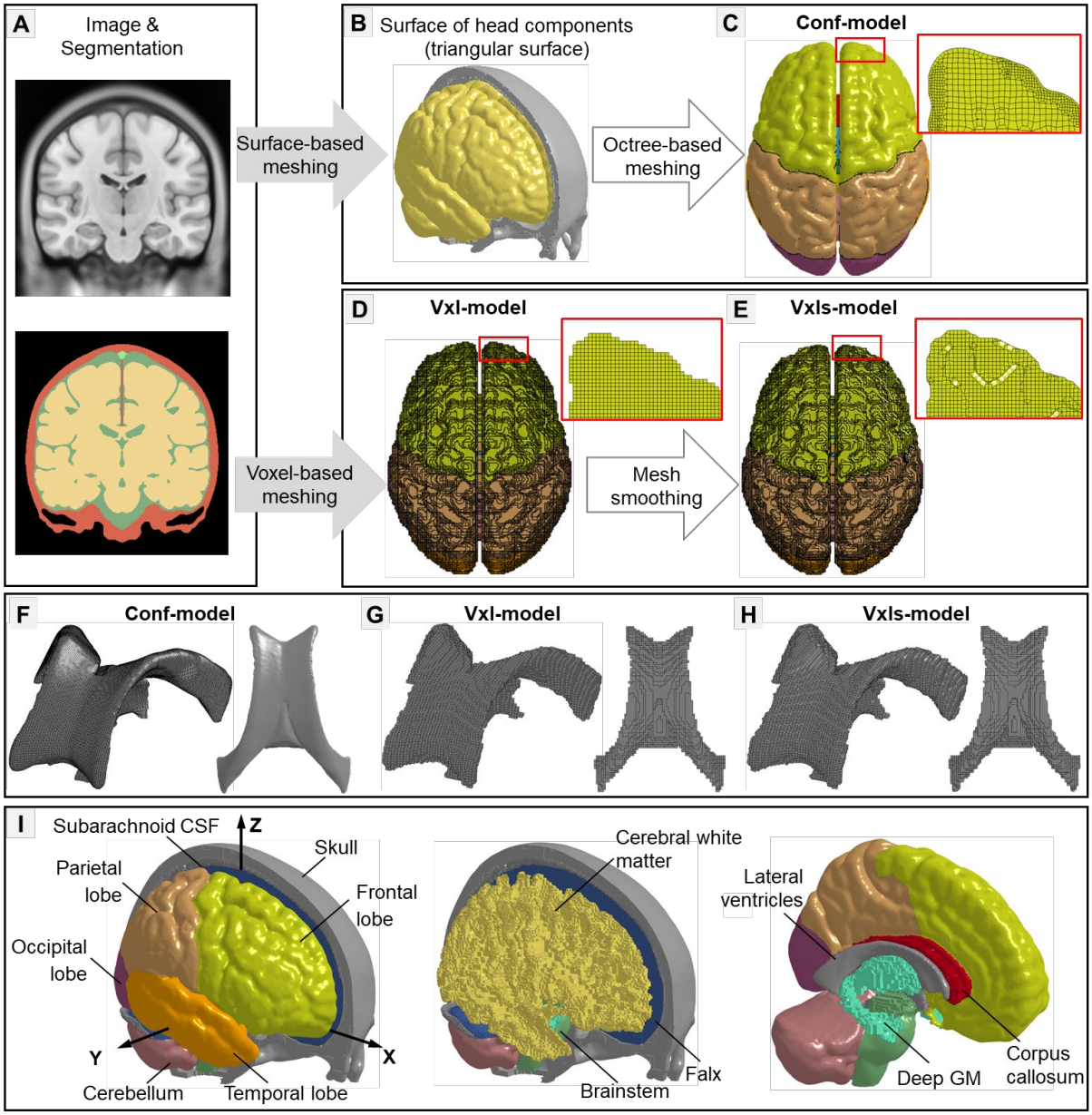

Fig 1. The workflow of developing three biomechanical head models with pure hexahedral meshes, named Conf-model (i.e., a model with conforming mesh for the brain-CSF interface), Vxl-model (i.e., a voxel-based model without mesh smoothing), and Vxls-model (i.e., a voxel-based model with mesh smoothing), respectively. (A) T1-weighted magnetic resonance imaging and corresponding segmentation. (B) The head geometries, i.e., skull, brain, and ventricle (unshown), were used to develop the Conf-model (C), while the segmentation was used to create the Vxl-model (D) and the Vxls-model (E). For the ventricles, an isometric view (mesh lines on) and a top view (mesh lines off) were provided for the Conf-model (F), Vxl-model (G), and Vxls-model. (H) To facilitate the post-processing, the brain elements of the three models were further grouped to have explicit representations of the major components (as exemplified by the Conf-model in subfigure I), including cerebral gray matter (GM) (i.e., frontal, parietal, occipital, and temporal lobes), cerebral white matter, deep GM (i.e., hippocampus and thalamus), corpus callosum, cerebellum, and brainstem. A skull-fixed coordinate system (XYZ, X: posterior-anterior; Y: left-right; Z: inferior-superior) was illustrated with the origin at head's center of gravity.

In the three models, the pia mater and dura mater were additionally created as shell elements by finding the outer surfaces of the brain and subarachnoid CSF, respectively. The falx and tentorium (shell elements) were manually generated based on the brain tissue classification and anatomical knowledge and matched in size among the three models. Except for stemming from the same imaging dataset for the head geometry as detailed above, the three models also shared commonalities in terms

of the material property, element formulation, and interface condition, as summarized in Appendix A in the current study and also detailed in the early article by Li, et al. [60]. In brief, the brain was modelled as a homogenous isotropic structure, but it was further grouped into different sub-components (Fig 1I) to facilitate postprocessing. The subarachnoid CSF and ventricles were modelled as an elastic fluid and shared interfacial nodes with the brain. A selectively reduced element formulation was used for the brain and CSF, circumventing the volume-locking phenomena and hourglass instability. Responses of the Conf-model have been extensively evaluated by experimental data of intracranial pressure, brain-skull relative displacement, brain strain, and strain rate [31, 60]. Additional validations of the Vxl- and Vxls-models were not performed, owing to the response similarity among the three models (see the results section).

Given its importance of numerical accuracy and stability, the mesh quality of the Conf-, Vxl-, and Vxls-models was examined based on 6 indices (pass/fail criteria), i.e., Jacobian (0.5), warpage (30°), skew (60°), aspect ratio (8), maximum angle (30°), and minimal angle (150°). These indices have been commonly used to assess mesh quality in the literature [21, 59, 65, 70] and the criterion of each index was the same as those adopted by Li, et al. [60].

Impact simulations

To compare the strain responses between the surface-based model and voxel-based models with and without smoothing, impact simulations were performed using Conf-, Vxl-, and Vxls-models. In one National Football League impact dataset, the head kinematics were obtained from laboratory reconstruction of on-field video-recorded collisions using Hybrid III anthropometric test dummies [76]. Ten cases, covering different impact directions and severities, were selected from this dataset. The acceleration peaks were summarized in Table 1 and detailed acceleration profiles of one representative case (i.e., Case 1) were exemplified in Figure 2. For each impact, the directional linear acceleration and angular velocity curves were imposed to one node located at the head's centre of gravity and constrained to the rigidly modelled skull. For a simulation of 60 ms, it took 8 hours for the Conf-model, 4 hours for the Vxl-model, and 5 hours for the Vxls-model, all of which were solved by the massively parallel processing version of LS-DYNA 13.0 version with 128 central processing units. The model responses were output at every 0.5 msec.

Table 1. Peaks of linear acceleration and angular acceleration of the 10 simulated cases. Note that the X, Y, and Z axes are the same as those in the skull-fixed coordinate system in Fig 1I.

Case ID	Peak linear acceleration (g)				Peak angular acceleration (krad/s^2)			
	X	Y	Z	Magnitude	X	Y	Z	Magnitude
Case 1	-42.3	114.3	-27.4	123.7	-3.53	-1.70	5.53	6.37
Case 2	-29.2	22.5	-34.6	49.4	-2.38	-1.01	1.10	2.77
Case 3	19.7	56.3	-6.0	59.8	-4.04	2.95	-6.74	8.30
Case 4	-21.5	59.4	-57.8	78.8	-5.82	1.66	2.43	6.23
Case 5	-31.9	-133.3	-41.6	138.2	4.65	1.35	6.82	7.50
Case 6	-78.0	66.5	-21.8	102.1	-3.21	-2.39	4.40	4.98
Case 7	-66.8	-20.0	-42.9	79.2	2.45	-3.44	-1.27	4.29

Case 8	-64.1	79.9	44.5	103.2	-5.69	-4.70	3.88	7.54
Case 9	-26.4	8.4	-13.5	29.3	-0.86	-1.41	-0.94	1.53
Case 10	-31.7	40.0	-18.2	52.3	-2.77	-1.87	-2.21	3.13

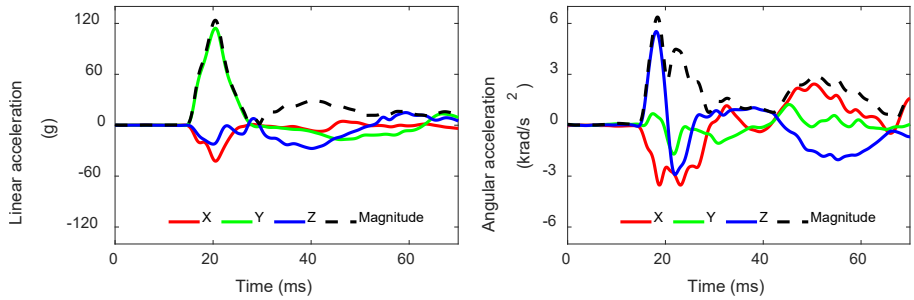

Fig 2. Acceleration curves for one representative impact (Case 1). Note that the X, Y, and Z axes are the same as those in the skull-fixed coordinate system in Fig 1F.

Strain analyses

To assess the influence of meshing techniques on strain responses, time-accumulated MPS values, regardless of the time of occurrence, were extracted directly from the simulations for each element (denoted as ε_{conf}^{sim} for the Conf-model, ε_{vxl}^{sim} for the Vxl-model, and ε_{vxls}^{sim} for the Vxls-model). Given the common suspicion that the FE head model, especially voxel-based meshing, was prone to have strain concentration [21, 24, 77], the maximum MPS value across all elements (determined by a single element with the highest MPS than its counterparts) was vulnerable to be affected by numerical artifacts. Instead, percentile MPS values (e.g., 99th percentile, 95th percentile, 90th percentile) were alternatively calculated. For example, the 95th percentile MPS was mathematically computed as the 95 percentile of element-wise MPS array (assuming the elements with MPS values in the top 5 percentile had numerical instability and should be excluded). Since no consensus was reached on the choice of percentile value [37, 78, 79], the strain values with the percentile ranging from 0 to 100 ('*prctile*' function in Matlab) were calculated. Note that the maximum MPS value across all elements was equivalent to the 100 percentile MPS value. In addition, the volume fraction of elements with the MPS magnitude over certain thresholds was also examined, similar to the widely used cumulative strain damage measure [80]. Both the magnitude- and volume-based calculations were implemented to the three models at four regions of interest (ROI), i.e., cerebral gray matter (GM) (including frontal, occipital, parietal, and temporal lobes), cerebral white matter (WM), CC, deep GM (including hippocampus and thalamus), and the whole brain level.

To further assess the similarity of strain patterns and localize the region with high strain differences among the three models, spatially detailed comparisons were performed based on voxelized strain results by mapping the element-wise brain MPS responses into the ICBM space (voxel resolution: 1 mm^3, brain voxels: 1567589). The mapped strain peaks were denoted as ε_{conf}^{map} for the Conf-model, ε_{vxl}^{map} for the Vxl-model, and ε_{vxls}^{map} for the Vxls-model. This mapping procedure was intuitive for the Vxl-Model and Vxls-Model owing to the one-one relationship between the element and the voxel.

Thereby, ε_{vxl}^{map} was identical to ε_{vxl}^{sim}, and ε_{vxls}^{map} was equivalent to ε_{vxls}^{sim}. For the Conf-model, the brain strain response was at the element level with spatially heterogeneous resolution, mismatching with the voxel resolution. To address this, the distances between voxels and elements were calculated. For a given voxel, its counterpart in the Conf-model was determined as the closest brain element in terms of Euclidean distance. The spatial deviations between paired voxels and elements were all less than 0.5 mm. As shown in Appendix B, identical distribution was noted between ε_{conf}^{sim} and ε_{conf}^{map}, supporting the validity of the voxelization procedure. Voxel-wise comparisons were performed among ε_{conf}^{map}, ε_{vxl}^{map}, and ε_{vxls}^{map} in an iterative manner. For any strain pairs, Pearson's correlation coefficient (R) was determined, and the root-mean-square error normalized by the mean value of the independent variables (NRMSD) was reported. The threshold for significance was $p < 0.05$.

Results

Strain responses

For one illustrative impact (Case 1), contours of element-wise MPS results directly from the Conf-, Vxl-, and Vxls-models (i.e., ε_{conf}^{sim}, ε_{vxl}^{sim}, and ε_{vxls}^{sim}) were qualitatively compared in Fig 3A-I. Remarkably similar strain patterns were noted among the three models with the high strain (characterized by red colour) commonly distributed at the peripherical area. A visual scrutinization of the enlarged view showed abrupt discontinuity in strain distribution at the cortex of the Vxl-model (Fig 3F), in which elements at the brain surface had much smaller strains than their underlying neighbouring counterparts. Such a discontinuity was less prominent in the Vxls-model (Fig 3I) and further mitigated in the Conf-model (Fig 3C).

For the magnitude-based strain comparisons, the cumulative percentile strain curves in Case 1 (Fig 3J) were generally overlaid with each other with exceptions noted at the 100th percentile value (both for the four ROIs and the whole brain). For example, the 100th percentile strain values in the cerebral GM were 0.63 for the Conf-model, 0.56 for the Vxl-model, and 0.59 for the Vxls-model. This was further confirmed in Fig 3K, in which the differences in the enumerated 99th, 95th, and 90th percentile strain peaks among the three models were less than 0.02. For Cases 2-10 (Fig 3L), similar trends were noted among the three models, of which the cumulative percentile strain curves were superimposed on each other with the disparity commonly noted in the 100th percentile value.

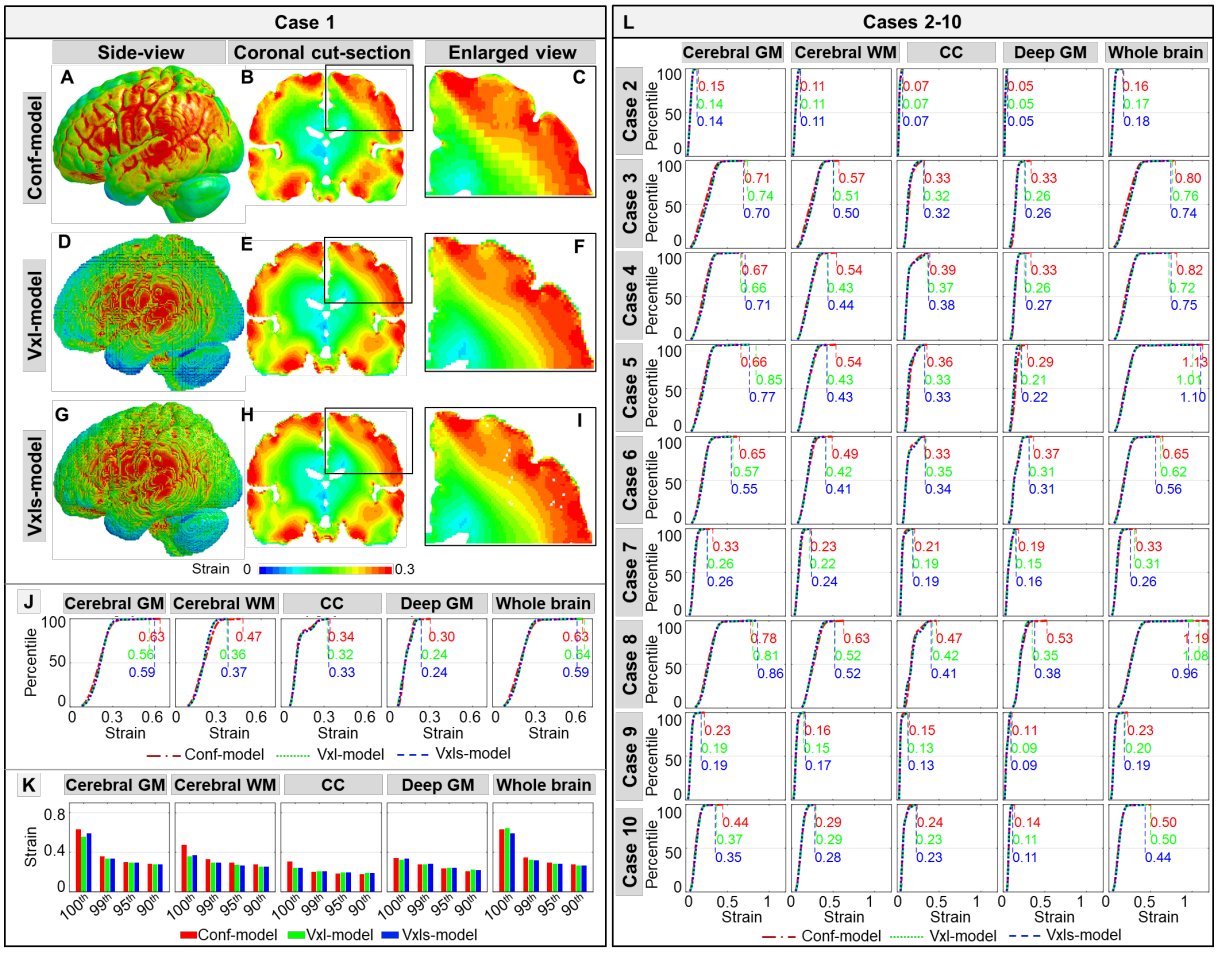

Fig 3. Comparisons of time-accumulated strain results among the Conf-, Vxl- and Vxls-models in Case 1 (A-K) and Cases 2-10 (L). For Case 1, strain results of the Conf-model were shown in the whole-brain side view (A), a coronal cut-section (B), and an enlarged view (C). Similar illustrations were presented for the Vxl-model (D-F) and Vxls-model (G-I). (J) Cumulative percentile strain curves at four regions of interest (i.e., cerebral gray matter (GM), cerebral white matter (WM), corpus callosum (CC), deep GM) and the whole brain in Case 1, of which the 100th percentile strain peak values were listed. (E) The strain peak values of 100th percentile, 99th percentile, 95th percentile, and 90th percentile in Case 1. (F) Cumulative percentile strain curves at four regions of interest and the whole brain in Cases 2-10 with the 100th percentile strain peaks listed. Note that all the strain results were directly extracted from the simulations.

For volume-based strain comparisons, comparable values were noted among the three models in terms of the volume fraction of elements with the MPS value over 0.2 for Case 1 (Fig 4A). The cross-model differences were less than 4%. For example, 16.2% of CC volume in the Conf-model endured a MPS value over 0.2, in contrast to 13.0% in the Vxl-model and 12.7% in the Vxls-model. When expanding to other strain thresholds and other impacts, curves that quantified the volume fractions of elements with the MPS value over different thresholds were largely overlaid among the three models (Fig 4B).

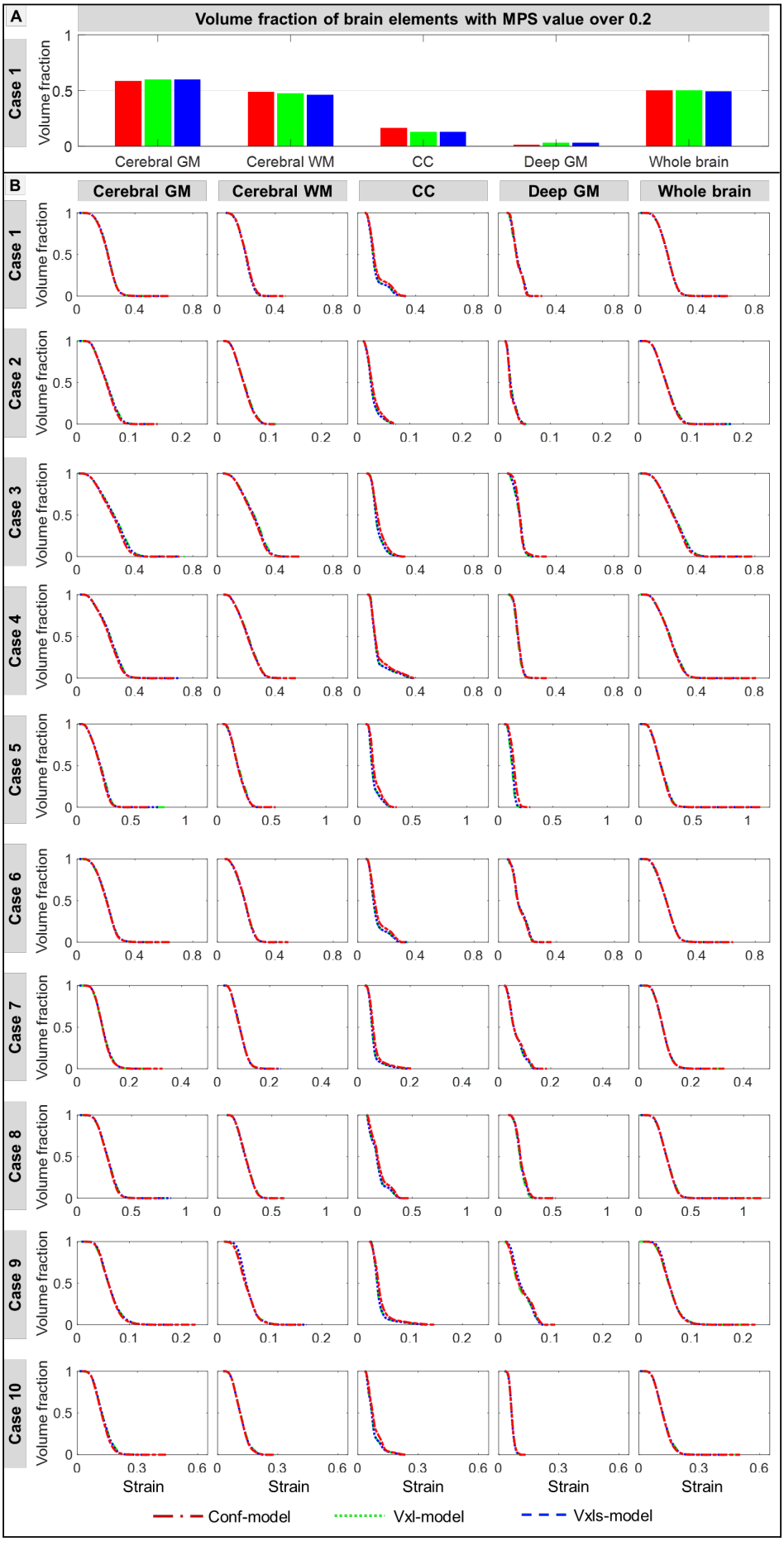
A
Volume fraction of brain elements with MPS value over 0.2
Case 1
Volume fraction
Cerebral GM
Cerebral WM
CC
Deep GM
Whole brain
B
Case 1
Case 2
Case 3
Case 4
Case 5
Case 6
Case 7
Case 8
Case 9
Case 10
Strain
Conf-model
Vxl-model
Vxls-model

Fig 4. (A) Volume fraction of brain elements with MPS value over 0.2 in cerebral gray matter (GM), cerebral white matter (WM), corpus callosum (CC), deep GM, and the whole brain estimated by the Conf-, Vxl- and Vxls-models in Case 1. (B) Cumulative curves of volume fraction of the elements with the strain over varying thresholds in ten impacts (i.e., Cases 1-10). These curves were calculated in the cerebral GM, cerebral WM, CC, deep GM, and whole brain. It should be clarified that, when the threshold was chosen as the 100th percentile strain of one model, the volume fractions among the three model would be different. As the resultant volume fractions were all close to or equal to zero, this threshold choice made little sense and hence was not discussed later.

When switching to the voxelized strain response (i.e., ε_{conf}^{map} for the Conf-model, ε_{vxl}^{map} for the Vxl-model, and ε_{vxls}^{map} for the Vxls-model), an illustrative comparison for Case 1 was shown in Fig 5A-F. The largest disparity was noted between ε_{conf}^{map} and ε_{vxl}^{map} with the R-value as 0.91 and the NRMSD as 11.7% (Fig 5A). Voxels with high strain differences (i.e., the absolute value of strain difference over 0.1) had a volume of 13.5 mL (vs. volume of all brain voxels as 1 568 mL) and were primarily located at interfacial boundaries (i.e., sulci and gyri in the cortex, regions adjacent to the falx and tentorium) in a cluster manner (Fig 5B). When switching to the strain pair of ε_{conf}^{map} and ε_{vxls}^{map}, the R-value was increased to 0.94 (NRMSD: 9.5%) (Fig 5C). The volume of voxels with high strain differences was 5.1 mL and those voxels were primarily aggregated around the tentorium and spread the whole pial surface in a dotted manner (Fig 5D). For the correlation between ε_{vxls}^{map} and ε_{vxl}^{map}, the R-value was 0.98 (NRMSD: 5.4%) (Fig 5E). Only a handful of voxels (primarily around the lateral sulcus) had strain differences over 0.1 (volume: 0.8 mL) (Fig 5F). When collectively scrutinizing ε_{conf}^{map}, ε_{vxl}^{map}, and ε_{vxls}^{map}, no consistent findings were noted regarding their relative magnitudes as both positive and negative values were noted in the subtraction of any strain pairs (Fig 5A-F).

Results of voxel-wise strain comparisons in all ten cases were summarized in Fig 5G. Similar to the findings noted in Case 1, the largest strain difference was observed from the strain pair of ε_{conf}^{map} and ε_{vxl}^{map} (R: 0.90 ~ 0.95, NRMSD: 10.5 ~ 13.1%), followed by the pair of ε_{conf}^{map} and ε_{vxls}^{map} (R: 0.92 ~ 0.96, NRMSD: 8.4 ~ 11.2%). The smallest difference was noted between ε_{vxls}^{map} and ε_{vxl}^{map} (R: 0.96 ~ 0.99, NRMSD: 4.3 ~ 8.2%).

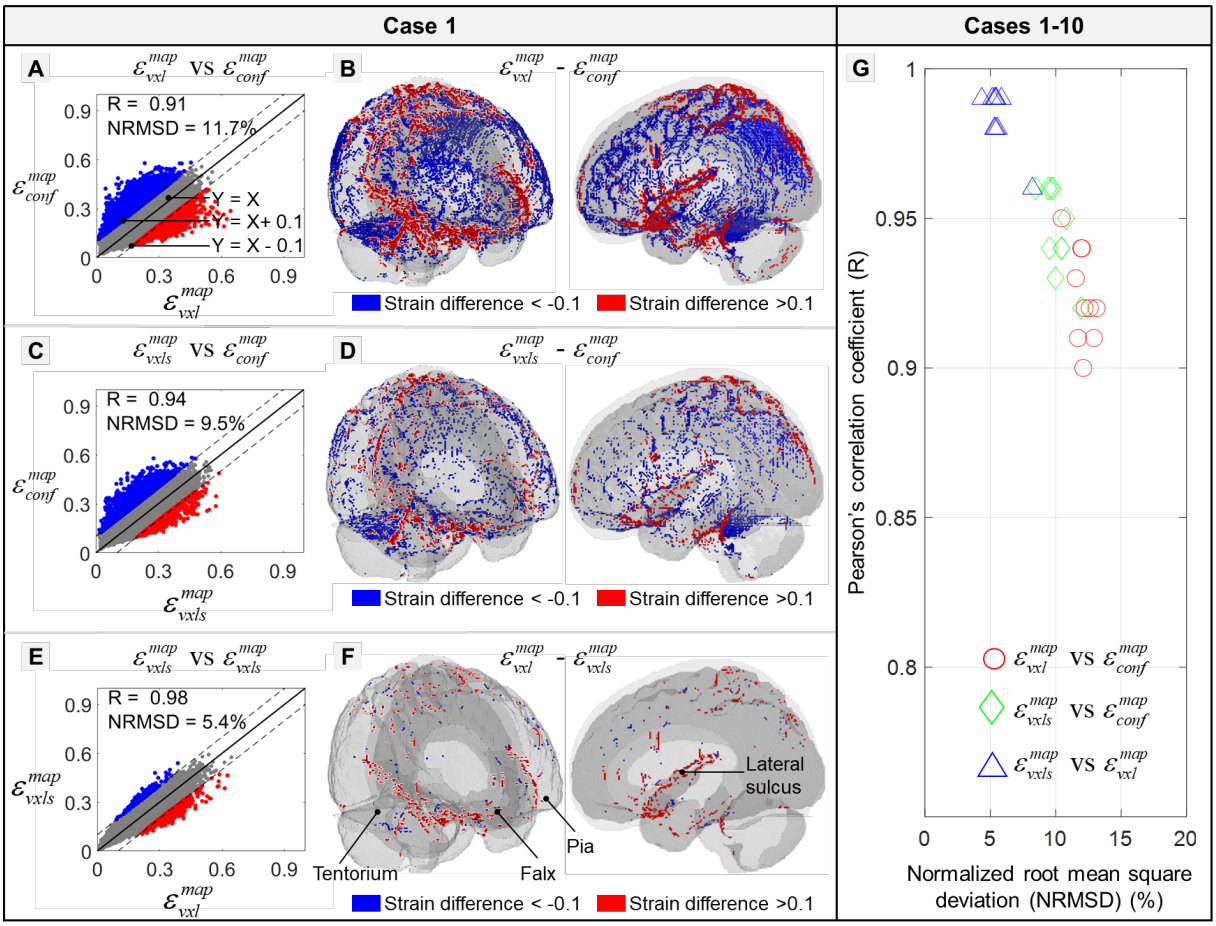

Fig 5. Comparisons of voxel-wise strain results among the Conf-, Vxl- and Vxls-models in Case 1 (A-F) and the Pearson's correlation coefficient (R) and normalized root mean square deviation (NRMSD) in Cases 1-10 were summarized (G). (A) Scatter plots of voxel-wise strains estimated by Conf-model and Vxl-model. Those elements with high strain difference (i.e., the strain difference was either larger than 0.1 (in red) or less than -0.1 (in blue)) were plotted in isometric and side views in subfigure (B). To help the reader better perceive the location of these identified elements, the pia mater (light gray), falx, and tentorium (dark gray) were shown in half transparency in subfigure B. Similar plots were also presented between the Conf-model and Vxls-model in subfigures (C)-(D), and between the Vxls-model and Vxl-model in subfigures (E)-(F). Note that all the strain results were mapped to the ICBM space.

Element quality

The Conf-, Vxl-, and Vxls-models varied in terms of element numbers and size (Table 2A). The Conf-model consisted of 4 612 951 solid elements (element size range: 0.1 ~ 3.8 mm). The Vxl- and Vxls-models had the same element number (i.e., 2 116 684). For the element size, a uniform size of 1 mm was noted in the Vxl-model and a range of 0.4 mm to 1.3 mm was measured from the Vxls-model. The histogram of element size distributions was available in Appendix C.

The element quality of three models based on 6 indices was summarized in Table 2B. All elements in the Vxl-mode were perfect cubes and all quality indexes were fully scored (e.g., Jacobian: 1). The mesh smoothing procedure reduced the element quality in the Vxls-model. For example, the minimum Jacobian was 0.13 and only 91% of elements had a Jacobian over 0.5. When switching to surface-based meshing, Jacobian, skew, aspect ratio, and element angles fell within the desirable ranges, with over 98% of elements exceeding the criteria. For example, over 98% of elements in the Conf-model

had a Jacobian over 0.5 with the minimum as 0.45. The only exception was noted in the warpage, in which only 92% of elements passed the criterion (i.e., warpage ≤ 30°) with the maximum as 111.8°. Detailed histograms of mesh quality were reported in Appendix C.

Table 2. Element number and element quality in the Conf-, Vxl-, and Vxls-models. (A) Element number and size range of brain, subarachnoid cerebrospinal fluid (CSF), ventricle and whole head. (B) Element quality based on six indices, each of which the percentage of elements passing with criteria (e.g., 0.5 for Jacobian) and minimum value were listed.

(A)	**Element number (range of element size)**			
Model	***Brain***	***Subarachnoid CSF***	***Ventricle***	***Whole head***
Conf-model	1 513 198 (0.1 ~ 3.8)	1 483 377 (0.2 ~ 2.3)	85 795 (0.2 ~ 1.9)	4 612 951 (0.1 ~ 3.8)
Vxl-model	1 567 589 (1)	520 041 (1)	29 054 (1)	2 116 684 (1)
Vxls-model	1 567 589 (0.4 ~ 1.3)	520 041 (0.4 ~ 1.4)	29 054 (0.4 ~ 1.4)	2 116 684 (0.4 ~ 1.4)

(B)	**Element quality index**											
Model	***Jacobian ≥ 0.5***		***Warpage (°) ≤ 30***		***Skew (°) ≤ 60***		***Aspect ratio ≤ 8***		***Min. angle (°) ≥ 30***		***Max angle (°) ≤ 150***	
	percent	Min.	percent	Max.	percent	Max.	percent	Max.	percent	Min.	percent	Max.
Conf-model	98%	0.45	92%	111.8	99.9%	70.0	99.9%	6.6	99.8%	18.0	99.9%	161.9
Vxl-model	100%	1	100%	0	100%	0	100%	1	100%	90	100%	90
Vxls-model	91%	0.13	87%	83.5	100%	42.5	100%	3.0	100%	44.7	97%	158.1

Discussion

The current study analysed the strain responses from three high-resolution, anatomically detailed head models, including one previously developed surface-based model with conforming elements for the brain-CSF interface [60] and two new models created from voxel-based meshing with and without smoothing. The results showed remarkably similar strain responses between the surface- and voxel-based models. When examining commonly used injury metrics, including the percentile strains below the maximum (e.g., 95 percentile strain) and volume fraction of brain elements with the strain over pre-defined thresholds, the responses of the three models were virtually equivalent. When scrutinizing the strain distribution, the three models showed different patterns at the interfacial boundary (e.g., sulci and gyri in the cortex, regions adjacent to the falx and tentorium) with strain differences over 0.1. The mesh smoothing procedure applied to the voxel-based model marginally reduced the strain discrepancies compared to the surface-based model. This study quantified the general similarity of strain responses between the surface- and voxel-based models and highlighted that caution should be exercised when interpreting the strain at the interface.

Considerations of cross-model strain comparison

While comparing the strain responses among the three models, such as the non-100 percentile strain value (e.g., 95 percentile strain values to exclude the top 5 extremely deformed brain elements)

(Fig 3) and volume fraction of brain elements with the strain magnitude over a certain threshold (Fig 4), virtually identical results were found between the surface- and voxel-based models with exceptions noted at the interfacial regions (Fig 5). Such findings correlated well with one early mouse study [81]. In 2022, Bradfield [81] created two FE head models of the mouse to virtually simulate experimental impacts, in which one model possessed conforming meshes to capture the pial surface and the other was voxelized from the imaging segmentation without smoothing (analogous to the Conf-model and Vxl-model, respectively, developed herein). Similar to the current results, remarkably similar spatial strain distributions were noted between these two mouse models with some strain discontinuities noted at the brain cortex. Considering that the mouse is a lissencephalic species without the gyri and sulci, this study could be regarded as a significant extension to the previous effort by focusing on the human brain (gyrencephalic) with sophisticated integrations of the intricated foldings of the cerebral cortex and complex profiles of the ventricle systems. The general consistency between these two independent studies involving two species highlighted the credibility of the presented results.

The general similarity in brain strain response among the Conf-, Vxl-, and Vxls-models could be explained by their comparable element number for the brain as well as other identical numerical settings. For the brain mesh size, several previous studies highlighted its influence on the brain strain [21-24, 81]. For example, Giudice, et al. [24] created a series of voxel models (without smoothing) and found reducing the element size from 4 mm to 1 mm increased the MPS (95th percentile values) from 0.33 to 0.77. In light of this, the element number for the brain was deliberately ensured to be comparable among the three models (i.e., 1 513 198 for the Conf-model vs. 1 567 589 for the Vxl- and Vxls-models, Table 2A). Consequently, the average element sizes in the three models were all around 1 mm, although the exact distribution of element sizes was different due to inherent disparities in surface-based and voxel-based meshing techniques and the involvement of mesh smoothing (Appendix C). The three models were further harmonized in terms of other major determinants of brain responses, including geometric resources, material properties, element formulations, and interfacial conditions (Appendix A). Such a study design enabled a focused investigation on the influence of three rival meshing techniques on brain strain responses. Responses among the three models were extensively evaluated via qualitative visualization of strain contours (Fig 3A-I), quantitative metrics including cumulative percentile strain value (Fig 3J-L), cumulative volume fractions of the brain with MPS over different thresholds (Fig 4), and spatially detailed, voxel-wised strain comparisons (Fig 5). Our multi-aspect assessment protocol collectively verified the brain strain responses between surface- and voxel-based models were generally comparable.

The disparity in brain strain between the surface- and voxel-based models at the interfacial boundary was related to the geometric inaccuracies introduced by voxel-based meshing. Despite the three models being derived from the same imaging dataset, the surface-based model deployed conforming elements to precisely capture the input surfaces (i.e., brain, subarachnoid CSF, ventricles,

and skull), while the voxel-based meshing, even with the smoothing operation, suffered from the intrinsic limitation of jagged interfaces between different tissues. Such a fundamental difference in resolving the geometrical complexity led to disparent strain responses at the interfacial region. Moreover, the mesh topologies between the surface- and voxel-based meshing were different (as exemplified by the enlarged views in Fig 1C vs. Fig 1D vs. Fig1E). Strain responses in the interfacial region with abrupt stiffness changes might be particularly sensitive to the localized mesh characteristics. For the brain-subarachnoid CSF interface, the brain was modelled as a hyper-viscoelastic material with a shear modulus of around 1 kPa, while the CSF as a nearly incompressible solid with low-shear resistance. For the falx-interhemispheric CSF-brain interfaces, the stiffness of the falx (Young's modulus: ~ 31.5 MPa) was much higher than those of the brain and CSF. When comparing the predicted strain between the Conf-model (conforming meshes for the cortical folds-subarachnoid CSF interface, Fig 1C) and Vxl-model (stair-stepped interface, Fig 1D), the brain elements with high strain difference were distributed at the site with shape stiffness gradient. The response dependency on the localized mesh topology at the region with material change has been previously reported in other TBI-related studies (e.g., cortical strain in the mouse brain [81] and human brain [24], pressure at the boundaries between different regions in blast-related head trauma [82]) and even beyond the TBI context (e.g., strain energy density in a compressed metal plate with an air-filled hole [83], bladder deformation in response to the urinary pressure [84], etc).

The current study also found that the mesh smoothing marginally mitigated the strain difference between the surface- and voxel-based models. This was supported by the subtle variations in the R-values of voxel-wise strain correlations, i.e., 0.90 ~ 0.95 between Conf-model and Vxl-model vs. 0.92 ~ 0.96 between Conf-model and Vxls-model. Such a finding could be explained from two perspectives. First, although the mesh smoothing reduced the jaggedness level at the brain-CSF interface, the resultant profiles of the brain and ventricle in the Vxls-mode were still not identical to those in the Conf-model. Second, the mesh topology in the surface- and voxel-based meshing was disparate, which was speculated to be the dominant factor responsible for the strain differences between the Conf- and Vxls-models, as discussed above. This speculation was verified by the high correlations of the strain responses (R: 0.96 ~ 0.99) between the Vxl- and Vxls-models, as both models shared identical mesh topologies.

Evidently, the surface-based model was anatomically more authentic than the voxel-based models in terms of capturing the smoothing feature of the cortical folds-subarachnoid CSF and brain-ventricle interfaces of the human brain. However, no experimental data were available to support the investigation on which model had more biofidelic interfacial responses. As elaborated by Li, et al. [60] and Zhou, et al. [31], the responses of the Conf-model were validated by experimental data in terms of brain motion [28], strain [29], and strain rate [31] that were measured from sites away from the ventricles and cortex. This was also the case in other available experimental data [27, 32, 33, 85]. In

two promising exceptions, Mallory [86] and Tesny [34] used ultrasound transducers to measure the relative motion between the brain cortex and skull by imposing sagittal head rotations on cadaveric heads. However, the accuracy of reported motion data in these two studies seemed to be compromised by various compounding factors (e.g., post-mortem time, storage temperature, etc) [34, 87]. Despite their uniqueness, these experimental datasets were not used to validate the cortical responses of FE head models in the current study. Another way of assessing the model-predicted results was to evaluate their predictability of injury. However, to the best of the authors' knowledge, no real-life human injury dataset existed with definitive brain pathology at the interfacial boundaries paired with accurate measurement of impact kinematics. It was also worth mentioning that the aforementioned issue was not necessarily specific to the current study and, instead, represented a challenge in the TBI research field.

The overt differences in interfacial strains among the Conf-, Vxl-, and Vxls-models, together with the unavailabilities of experimental data and injury dataset for the investigation of interfacial responses as detailed above, collectively underscored that caution should be exercised when the strain at the interface was the response of interest. For example, using voxel-based head models with mesh smoothing, Ho and Kleiven [46] found high strain at the depth of the sulci largely overlapped with the site of tau pathology in chronic traumatic encephalopathy. Despite interesting initial findings, further verifications were necessary by involving other advanced head models, e.g., the anatomically more authentic Conf-model [60].

Considerations of mesh techniques and element quality

For the Conf-model and Vxls-model developed herein, the element quality was largely comparable to existing FE models [21, 23, 56, 57, 59, 65]. For example, in one voxel-based head model [65] with mesh smoothing and the cortical folds and ventricles being preserved, the most distorted element has a Jabocian of 0.23, inferior to the Conf-model (minimum Jacobian: 0.45) and superior to the Vxls-model (minimum Jacobian: 0.13). In another FE head model (average element size: ~ 1.1 mm) without the gyri and sulci [23], the minimum and maximum angles were 11.8° and 176.3°, in comparison to 18.0° and 161.9° in the Conf-model, 44.7° and 158.1° in the Vxls-model. For the Vxl-model developed here and its other counterparts in the literature [39, 62-64], all elements were perfect cubes with idealized mesh qualities.

For the surface-based meshing, to the best of the authors' knowledge, only the Conf-model [60] and a few other models developed by the same research group [50, 51, 60] employed pure hexahedral meshes to discretize the whole head with the cortical folds and ventricles preserved. For the voxel-based meshing without smoothing, it has been leveraged by several groups to develop head models with stair-like interfaces [39, 62-64]. When it came to the meshing smoothing, the choice of one Laplacian-based, volume-preserving meshing algorithm in the current study was justified by the

availability of the technique details elaborated by Boyd and Müller [75] and its early implementation to smooth voxel-based FE models for brain research [46, 66]. In the study by Chen and Ostoja-Starzewski [66] in which the mesh in a voxelized whole-head model was smoothed, element quality statistics were not reported, prohibiting a direct comparison to the Vxls-model in the current study. In the other study by Kelley, et al. [70], the mesh smoothing was only applied to brain sections (i.e., partitioning the brain into eight sections with the size of each section around one-eighth of the whole brain), instead of the whole-head level as is the case of the Vxls-model in the current study. It was also noted that the exact details of the smoothing procedure were omitted in a few studies [67, 68] while developing voxel-based FE human head models.

Other limitations and paths forward

Several other limitations, except for the few highlighted above, should be acknowledged with further investigations deemed necessary. First, the current study approximated the brain as a homogeneous structure, as no consensus has been reached yet regarding the regional trend of brain stiffness which seemed to be compounded by various factors (e.g., loading rate, drainage conditions, length scale, etc) [88]. Future work could plant region-wise material constants, when more consensual results were avaialble, to the FE head model with meshes conforming to the material boundaries [89]. Second, the CSF was simplified as a Lagrangian-based solid structure with low shear stiffness, as was also the case in other FE head models [14, 24, 39, 46, 62-68, 77]. Emerging efforts have been noted in implementing arbitrary Lagrangian-Eulerian (ALE) fluid elements for the ventricle [50, 51]. Such an implementation could be expanded to subarachnoid CSF, although the enormously high computational expense per solving the ALE formulation [90] was expected to be a bottleneck. Beyond the three rival techniques presented herein, extra hexahedral meshing approaches were available, e.g., the multi-block approach that was prevalently used in the biomechanical field [21, 23, 57, 59, 81, 91-95]. However, the multi-block approach has not succeeded yet in developing hexahedral-based head models with details such as gyri and sulci retained and hence were not included in the current study.

Conclusion

The current study performed strain comparisons among three anatomically detailed FE head model models. One was previously developed from surface-based meshing with conforming elements for the cortical folds-subarachnoid CSF and brain-ventricle interfaces [60], while the other two were newly created by converting the segmented voxels into elements with and with mesh smoothing. It was verified that the strain responses between the surface- and voxel-based models were largely comparable with exceptions at the interfacial region (e.g., sulci and gyri in the cortex, regions adjacent to the falx and tentorium) where strain differences over 0.1 were noted. By scrutinizing the commonly used injury metrics, including the percentile strain below the maximum (e.g., 95 percentile strain) and the volume fraction of brain elements with strains over certain thresholds, the responses of the three

models were virtually identical. The smoothing procedure marginally mitigated the strain differences between the surface- and voxel-based models. This study provided quantitative insights into how close the strain responses were between the surface- and voxel-based FE head models and highlighted the importance of exercising caution when using strain at the interface to predict injury.

Acknowledgement

This research has received funding from KTH Royal Institute of Technology (Stockholm, Sweden), the Swedish Governmental Agency for Innovation Systems (VINNOVA) (no. 2023-00753), Swedish Research Council (VR-2020-04496 and VR-2020-04724), Skyltfonden from the trafiksäkerhet (TRV 2024/23811), and the Torvald and Britta Gahlin's foundation. The content of this article is solely the responsibility of the authors and does not necessarily represent the official views of neither funding agencies. The computational simulations were enabled by resources provided by the National Academic Infrastructure for Supercomputing in Sweden (NAISS) at the center for High Performance Computing (PDC) partially funded by the Swedish Research Council through grant agreement no. 2022-06725. The authors declare that they have no known competing financial interests or personal relationships that could have appeared to influence the work reported in this paper.

References

[1] M. C. Dewan, A. Rattani, S. Gupta, R. E. Baticulon, Y.-C. Hung, M. Punchak, A. Agrawal, A. O. Adeleye, M. G. Shrime, and A. M. Rubiano, "Estimating the global incidence of traumatic brain injury," *Journal of neurosurgery,* vol. 130, no. 4, pp. 1080-1097, 2018.
[2] A. Brazinova, V. Rehorcikova, M. S. Taylor, V. Buckova, M. Majdan, M. Psota, W. Peeters, V. Feigin, A. Theadom, and L. Holkovic, "Epidemiology of traumatic brain injury in Europe: a living systematic review," *Journal of neurotrauma,* vol. 38, no. 10, pp. 1411-1440, 2021.
[3] A. I. Maas, D. K. Menon, G. T. Manley, M. Abrams, C. Åkerlund, N. Andelic, M. Aries, T. Bashford, M. J. Bell, and Y. G. Bodien, "Traumatic brain injury: progress and challenges in prevention, clinical care, and research," *The Lancet Neurology,* vol. 21, no. 11, pp. 1004-1060, 2022.
[4] W. Peeters, R. van den Brande, S. Polinder, A. Brazinova, E. W. Steyerberg, H. F. Lingsma, and A. I. Maas, "Epidemiology of traumatic brain injury in Europe," *Acta neurochirurgica,* vol. 157, pp. 1683-1696, 2015.
[5] J. Olesen, A. Gustavsson, M. Svensson, H. U. Wittchen, B. Jönsson, C. S. Group, and E. B. Council, "The economic cost of brain disorders in Europe," *European journal of neurology,* vol. 19, no. 1, pp. 155-162, 2012.
[6] A. I. Maas, D. K. Menon, P. D. Adelson, N. Andelic, M. J. Bell, A. Belli, P. Bragge, A. Brazinova, A. Büki, and R. M. Chesnut, "Traumatic brain injury: integrated approaches to improve prevention, clinical care, and research," *The Lancet Neurology,* vol. 16, no. 12, pp. 987-1048, 2017.
[7] S. Ji, M. Ghajari, H. Mao, R. H. Kraft, M. Hajiaghamemar, M. B. Panzer, R. Willinger, M. D. Gilchrist, S. Kleiven, and J. D. Stitzel, "Use of brain biomechanical models for monitoring impact exposure in contact sports," *Annals of Biomedical Engineering,* vol. 50, no. 11, pp. 1389-1408, 2022.
[8] S. Kleiven, "Finite element modeling of the human head," KTH, 2002.
[9] J. S. Giudice, T. J. Druzgal, and M. B. Panzer, "Investigating the Effect of Brain Size on Deformation Magnitude Using Subject-Specific Finite Element Models," *Journal of Neurotrauma,* vol. 40, no. 15-16, pp. 1796-1807, 2023.
[10] S. Kleiven, and H. Von Holst, "Consequences of head size following trauma to the human head," *Journal of biomechanics,* vol. 35, no. 2, pp. 153-160, 2002.

[11] X. Li, "Subject-specific head model generation by mesh morphing: A personalization framework and its applications," *Frontiers in bioengineering and biotechnology,* vol. 9, pp. 706566, 2021.
[12] R. Cloots, H. Gervaise, J. Van Dommelen, and M. Geers, "Biomechanics of traumatic brain injury: influences of the morphologic heterogeneities of the cerebral cortex," *Annals of biomedical engineering,* vol. 36, pp. 1203-1215, 2008.
[13] C. Giordano, R. Cloots, J. Van Dommelen, and S. Kleiven, "The influence of anisotropy on brain injury prediction," *Journal of biomechanics,* vol. 47, no. 5, pp. 1052-1059, 2014.
[14] J. Ho, Z. Zhou, X. Li, and S. Kleiven, "The peculiar properties of the falx and tentorium in brain injury biomechanics," *Journal of biomechanics,* vol. 60, pp. 243-247, 2017.
[15] X. Li, H. Sandler, and S. Kleiven, "The importance of nonlinear tissue modelling in finite element simulations of infant head impacts," *Biomechanics and modeling in mechanobiology,* vol. 16, pp. 823-840, 2017.
[16] W. Zhao, B. Choate, and S. Ji, "Material properties of the brain in injury-relevant conditions–Experiments and computational modeling," *Journal of the mechanical behavior of biomedical materials,* vol. 80, pp. 222-234, 2018.
[17] Z. Zhou, X. Li, and S. Kleiven, "Fluid–structure interaction simulation of the brain–skull interface for acute subdural haematoma prediction," *Biomechanics and modeling in mechanobiology,* vol. 18, pp. 155-173, 2019.
[18] Z. Zhou, X. Li, and S. Kleiven, "Evaluation of brain-skull interface modelling approaches on the prediction of acute subdural hematoma in the elderly," *Journal of biomechanics,* vol. 105, pp. 109787, 2020.
[19] F. Wang, Y. Han, B. Wang, Q. Peng, X. Huang, K. Miller, and A. Wittek, "Prediction of brain deformations and risk of traumatic brain injury due to closed-head impact: quantitative analysis of the effects of boundary conditions and brain tissue constitutive model," *Biomechanics and Modeling in Mechanobiology,* vol. 17, pp. 1165-1185, 2018.
[20] A. Rycman, M. Bustamante, and D. S. Cronin, "Brain Material Properties and Integration of Arachnoid Complex for Biofidelic Impact Response for Human Head Finite Element Model," *Annals of Biomedical Engineering*, pp. 1-12, 2024.
[21] H. Mao, H. Gao, L. Cao, V. V. Genthikatti, and K. H. Yang, "Development of high-quality hexahedral human brain meshes using feature-based multi-block approach," *Computer methods in biomechanics and biomedical engineering,* vol. 16, no. 3, pp. 271-279, 2013.
[22] M. B. Panzer, B. S. Myers, and C. R. Bass, "Mesh considerations for finite element blast modelling in biomechanics," *Computer methods in biomechanics and biomedical engineering,* vol. 16, no. 6, pp. 612-621, 2013.
[23] W. Zhao, and S. Ji, "Mesh convergence behavior and the effect of element integration of a human head injury model," *Annals of biomedical engineering,* vol. 47, pp. 475-486, 2019.
[24] J. S. Giudice, W. Zeng, T. Wu, A. Alshareef, D. F. Shedd, and M. B. Panzer, "An analytical review of the numerical methods used for finite element modeling of traumatic brain injury," *Annals of biomedical engineering,* vol. 47, pp. 1855-1872, 2019.
[25] E. G. Takhounts, R. H. Eppinger, J. Q. Campbell, R. E. Tannous, E. D. Power, and L. S. Shook, "On the Development of the SIMon Finite Element Head Model," *Stapp car crash journal,* vol. 47, pp. 107-133, 2003.
[26] A. Alshareef, J. S. Giudice, J. Forman, R. S. Salzar, and M. B. Panzer, "A novel method for quantifying human in situ whole brain deformation under rotational loading using sonomicrometry," *Journal of neurotrauma,* vol. 35, no. 5, pp. 780-789, 2018.
[27] A. Alshareef, J. S. Giudice, J. Forman, D. F. Shedd, K. A. Reynier, T. Wu, S. Sochor, M. R. Sochor, R. S. Salzar, and M. B. Panzer, "Biomechanics of the human brain during dynamic rotation of the head," *Journal of neurotrauma,* vol. 37, no. 13, pp. 1546-1555, 2020.
[28] W. N. Hardy, M. J. Mason, C. D. Foster, C. S. Shah, J. M. Kopacz, K. H. Yang, A. I. King, J. Bishop, M. Bey, and W. Anderst, "A study of the response of the human cadaver head to impact," *Stapp car crash journal,* vol. 51, pp. 17, 2007.
[29] Z. Zhou, X. Li, S. Kleiven, and W. N. Hardy, "Brain Strain from Motion of Sparse Markers," *Stapp car crash journal,* vol. 63, pp. 1-27, 2019.

[30] Z. Zhou, X. Li, S. Kleiven, C. Shah, and W. Hardy, "A reanalysis of experimental brain strain data: implication for finite element head model validation," *Stapp Car Crash Journal,* vol. 62, pp. 293-318, 2018.
[31] Z. Zhou, X. Li, Y. Liu, W. N. Hardy, and S. Kleiven, "Brain strain rate response: addressing computational ambiguity and experimental data for model validation," *Brain Multiphysics,* vol. 4, pp. 100073, 2023.
[32] W. Hardy, C. Foster, M. Mason, K. Yang, A. King, and S. Tashman, "Investigation of Head Injury Mechanisms Using Neutral Density Technology and High-Speed Biplanar X-ray," *Stapp car crash journal,* vol. 45, pp. 337-368, 2001.
[33] S. Dutrisac, J. Rovt, A. Post, S. Goodwin, G. O. Cron, A. Jalali, K. Poon, S. Brien, H. Frei, and T. B. Hoshizaki, "Intracranial displacement measurements within targeted anatomical regions of a postmortem human surrogate brain subjected to impact," *Annals of Biomedical Engineering,* vol. 49, pp. 2836-2851, 2021.
[34] A. C. Tesny, "Quantifying Relative Surface Level Brain Motion in Postmortem Human Subjects Using High-Frequency B-Mode Ultrasound," The Ohio State University, 2022.
[35] W. Zhao, and S. Ji, "White matter anisotropy for impact simulation and response sampling in traumatic brain injury," *Journal of neurotrauma,* vol. 36, no. 2, pp. 250-263, 2019.
[36] Z. Zhou, X. Li, Y. Liu, M. Fahlstedt, M. Georgiadis, X. Zhan, S. J. Raymond, G. Grant, S. Kleiven, and D. Camarillo, "Toward a comprehensive delineation of white matter tract-related deformation," *Journal of neurotrauma,* vol. 38, no. 23, pp. 3260-3278, 2021.
[37] M. Fahlstedt, S. Meng, and S. Kleiven, "Influence of strain post-processing on brain injury prediction," *Journal of Biomechanics,* vol. 132, pp. 110940, 2022.
[38] Z. Zhou, C. Olsson, T. C. Gasser, X. Li, and S. Kleiven, "The white matter fiber tract deforms most in the perpendicular direction during in vivo volunteer impacts," *bioRxiv*, pp. 2024.03. 26.585293, 2024.
[39] J. S. Giudice, A. Alshareef, T. Wu, C. A. Gancayco, K. A. Reynier, N. J. Tustison, T. J. Druzgal, and M. B. Panzer, "An image registration-based morphing technique for generating subject-specific brain finite element models," *Annals of Biomedical Engineering,* vol. 48, pp. 2412-2424, 2020.
[40] S. Kleiven, "Predictors for traumatic brain injuries evaluated through accident reconstructions," *Stapp car Crash Journal,* vol. 51, pp. 81-114, 2007.
[41] S. Ji, W. Zhao, J. C. Ford, J. G. Beckwith, R. P. Bolander, R. M. Greenwald, L. A. Flashman, K. D. Paulsen, and T. W. McAllister, "Group-wise evaluation and comparison of white matter fiber strain and maximum principal strain in sports-related concussion," *Journal of neurotrauma,* vol. 32, no. 7, pp. 441-454, 2015.
[42] A. Montanino, X. Li, Z. Zhou, M. Zeineh, D. Camarillo, and S. Kleiven, "Subject-specific multiscale analysis of concussion: from macroscopic loads to molecular-level damage," *Brain multiphysics,* vol. 2, pp. 100027, 2021.
[43] Q. Yuan, X. Li, Z. Zhou, and S. Kleiven, "A novel framework for video-informed reconstructions of sports accidents: A case study correlating brain injury pattern from multimodal neuroimaging with finite element analysis," *Brain Multiphysics,* vol. 6, pp. 100085, 2024.
[44] C. Zhang, L. Bartels, A. Clansey, J. Kloiber, D. Bondi, P. van Donkelaar, L. Wu, A. Rauscher, and S. Ji, "A computational pipeline towards large-scale and multiscale modeling of traumatic axonal injury," *Computers in Biology and Medicine*, pp. 108109, 2024.
[45] M. Fahlstedt, B. Depreitere, P. Halldin, J. Vander Sloten, and S. Kleiven, "Correlation between injury pattern and finite element analysis in biomechanical reconstructions of traumatic brain injuries," *Journal of biomechanics,* vol. 48, no. 7, pp. 1331-1335, 2015.
[46] J. Ho, and S. Kleiven, "Can sulci protect the brain from traumatic injury?," *Journal of Biomechanics,* vol. 42, no. 13, pp. 2074-2080, 2009.
[47] M. Ghajari, P. J. Hellyer, and D. J. Sharp, "Computational modelling of traumatic brain injury predicts the location of chronic traumatic encephalopathy pathology," *Brain,* vol. 140, no. 2, pp. 333-343, 2017.
[48] S. J. Strich, "Diffuse degeneration of the cerebral white matter in severe dementia following head injury," *Journal of neurology, neurosurgery, and psychiatry,* vol. 19, no. 3, pp. 163, 1956.

[49] A. C. McKee, T. D. Stein, C. J. Nowinski, R. A. Stern, D. H. Daneshvar, V. E. Alvarez, H.-S. Lee, G. Hall, S. M. Wojtowicz, and C. M. Baugh, "The spectrum of disease in chronic traumatic encephalopathy," *Brain,* vol. 136, no. 1, pp. 43-64, 2013.
[50] Z. Zhou, X. Li, and S. Kleiven, "Biomechanics of periventricular injury," *Journal of neurotrauma*, 2020.
[51] Z. Zhou, X. Li, A. G. Domel, E. L. Dennis, M. Georgiadis, Y. Liu, S. J. Raymond, G. Grant, S. Kleiven, and D. Camarillo, "The presence of the temporal horn exacerbates the vulnerability of hippocampus during head impacts," *Frontiers in Bioengineering and Biotechnology,* vol. 10, pp. 754344, 2022.
[52] Y. Makino, "Morphological changes of cerebral ventricular wall in traumatic brain injury evaluated via large histological specimens," *Journal of neurotrauma,* vol. 21, no. 5, pp. 585-594, 2004.
[53] H. Kimpara, Y. Nakahira, M. Iwamoto, K. Miki, K. Ichihara, S.-i. Kawano, and T. Taguchi, "Investigation of anteroposterior head-neck responses during severe frontal impacts using a brain-spinal cord complex FE model," *Stapp car crash journal,* vol. 50, pp. 509-544, 2006.
[54] E. G. Takhounts, S. A. Ridella, V. Hasija, R. E. Tannous, J. Q. Campbell, D. Malone, K. Danelson, J. Stitzel, S. Rowson, and S. Duma, "Investigation of traumatic brain injuries using the next generation of simulated injury monitor (SIMon) finite element head model," *Stapp car crash journal,* vol. 52, pp. 1-31, 2008.
[55] H. Mao, L. Zhang, B. Jiang, V. V. Genthikatti, X. Jin, F. Zhu, R. Makwana, A. Gill, G. Jandir, and A. Singh, "Development of a finite element human head model partially validated with thirty five experimental cases," *Journal of biomechanical engineering,* vol. 135, no. 11, pp. 111002, 2013.
[56] A. Trotta, J. M. Clark, A. McGoldrick, M. D. Gilchrist, and A. N. Annaidh, "Biofidelic finite element modelling of brain trauma: Importance of the scalp in simulating head impact," *International Journal of Mechanical Sciences,* vol. 173, pp. 105448, 2020.
[57] H. T. Garimella, and R. H. Kraft, "Modeling the mechanics of axonal fiber tracts using the embedded finite element method," *International journal for numerical methods in biomedical engineering,* vol. 33, no. 5, pp. e2823, 2017.
[58] L. Zhang, K. Yang, R. Dwarampudi, K. Omori, T. Li, K. Chang, W. Hardy, T. Khalil, and A. King, "Recent advances in brain injury research: a new human head model development and validation," *Stapp car crash journal,* vol. 45, pp. 369-394, 2001.
[59] Z. Zhou, B. Jiang, L. Cao, F. Zhu, H. Mao, and K. H. Yang, "Numerical simulations of the 10-year-old head response in drop impacts and compression tests," *computer methods and programs in biomedicine,* vol. 131, pp. 13-25, 2016.
[60] X. Li, Z. Zhou, and S. Kleiven, "An anatomically detailed and personalizable head injury model: Significance of brain and white matter tract morphological variability on strain," *Biomechanics and modeling in mechanobiology,* vol. 20, pp. 403-431, 2021.
[61] X. Li, H. Sandler, and S. Kleiven, "Infant skull fractures: Accident or abuse?: Evidences from biomechanical analysis using finite element head models," *Forensic science international,* vol. 294, pp. 173-182, 2019.
[62] A. Alshareef, A. K. Knutsen, C. L. Johnson, A. Carass, K. Upadhyay, P. V. Bayly, D. L. Pham, J. L. Prince, and K. Ramesh, "Integrating material properties from magnetic resonance elastography into subject-specific computational models for the human brain," *Brain Multiphysics,* vol. 2, pp. 100038, 2021.
[63] P. G. Pavan, M. Nasim, V. Brasco, S. Spadoni, F. Paoloni, D. d'Avella, S. F. Khosroshahi, N. de Cesare, K. Gupta, and U. Galvanetto, "Development of detailed finite element models for in silico analyses of brain impact dynamics," *Computer Methods and Programs in Biomedicine,* vol. 227, pp. 107225, 2022.
[64] L. E. Miller, J. E. Urban, and J. D. Stitzel, "Development and validation of an atlas-based finite element brain model," *Biomechanics and modeling in mechanobiology,* vol. 15, no. 5, pp. 1201-1214, 2016.
[65] J. Ho, H. von Holst, and S. Kleiven, "Automatic generation and validation of patient-specific finite element head models suitable for crashworthiness analysis," *International journal of crashworthiness,* vol. 14, no. 6, pp. 555-563, 2009.

[66] Y. Chen, and M. Ostoja-Starzewski, "MRI-based finite element modeling of head trauma: spherically focusing shear waves," *Acta mechanica,* vol. 213, no. 1-2, pp. 155-167, 2010.
[67] H. Duckworth, A. Azor, N. Wischmann, K. A. Zimmerman, I. Tanini, D. J. Sharp, and M. Ghajari, "A finite element model of cerebral vascular injury for predicting microbleeds location," *Frontiers in Bioengineering and Biotechnology,* vol. 10, pp. 860112, 2022.
[68] E. Griffiths, J. Hinrichsen, N. Reiter, and S. Budday, "On the importance of using region-dependent material parameters for full-scale human brain simulations," *European Journal of Mechanics-A/Solids,* vol. 99, pp. 104910, 2023.
[69] T. Wang, S. Kleiven, and X. Li, "Electroosmosis based novel treatment approach for cerebral edema," *IEEE Transactions on Biomedical Engineering,* vol. 68, no. 9, pp. 2645-2653, 2020.
[70] M. E. Kelley, L. E. Miller, J. E. Urban, and J. D. Stitzel, "Mesh Smoothing Algorithm Applied to a Finite Element Model of the Brain for Improved Brain-Skull Interface," *Biomedical Sciences Instrumentation,* vol. 51, pp. 181-188, 2015.
[71] V. Fonov, A. C. Evans, K. Botteron, C. R. Almli, R. C. McKinstry, D. L. Collins, and B. D. C. Group, "Unbiased average age-appropriate atlases for pediatric studies," *Neuroimage,* vol. 54, no. 1, pp. 313-327, 2011.
[72] L. Maréchal, "Advances in octree-based all-hexahedral mesh generation: handling sharp features." pp. 65-84.
[73] M. S. Shephard, and M. K. Georges, "Automatic three‐dimensional mesh generation by the finite octree technique," *International Journal for Numerical methods in engineering,* vol. 32, no. 4, pp. 709-749, 1991.
[74] R. Schneiders, "Octree-based hexahedral mesh generation," *International Journal of Computational Geometry & Applications,* vol. 10, no. 04, pp. 383-398, 2000.
[75] S. K. Boyd, and R. Müller, "Smooth surface meshing for automated finite element model generation from 3D image data," *Journal of biomechanics,* vol. 39, no. 7, pp. 1287-1295, 2006.
[76] E. J. Sanchez, L. F. Gabler, A. B. Good, J. R. Funk, J. R. Crandall, and M. B. Panzer, "A reanalysis of football impact reconstructions for head kinematics and finite element modeling," *Clinical biomechanics,* vol. 64, pp. 82-89, 2019.
[77] A. Madhukar, and M. Ostoja-Starzewski, "Finite element methods in human head impact simulations: a review," *Annals of biomedical engineering,* vol. 47, pp. 1832-1854, 2019.
[78] J. Östh, K. Bohman, and L. Jakobsson, "Head injury criteria assessment using head kinematics from crash tests and accident reconstructions," *Traffic injury prevention,* vol. 24, no. 1, pp. 56-61, 2023.
[79] M. B. Panzer, B. S. Myers, B. P. Capehart, and C. R. Bass, "Development of a finite element model for blast brain injury and the effects of CSF cavitation," *Annals of biomedical engineering,* vol. 40, pp. 1530-1544, 2012.
[80] E. Takhounts, S. Ridella, V. Hasija, R. Tannous, J. Campbell, D. Malone, K. Danelson, J. Stitzel, S. Rowson, and S. Duma, "Investigation of traumatic brain injuries using the next generation of simulated injury monitor (SIMon) finite element head model," *Stapp car Crash Journal,* vol. 52, pp. 1-31, 2008.
[81] C. A. Bradfield, "Traumatic axonal injury in the mouse brain," Johns Hopkins University, 2022.
[82] X. Yu, and M. Ghajari, "An assessment of blast modelling techniques for injury biomechanics research," *International Journal for Numerical Methods in Biomedical Engineering,* vol. 35, no. 12, pp. e3258, 2019.
[83] R. Guldberg, S. Hollister, and G. Charras, "The accuracy of digital image-based finite element models," 1998.
[84] X. Chai, M. van Herk, M. C. Hulshof, and A. Bel, "A voxel‐based finite element model for the prediction of bladder deformation," *Medical physics,* vol. 39, no. 1, pp. 55-65, 2012.
[85] A. J. Guettler, R. Ramachandra, J. Bolte, and W. N. Hardy, *Kinematics response of the PMHS brain to rotational loading of the head: Development of experimental methods and analysis of preliminary data,* 0148-7191, SAE Technical Paper, 2018.
[86] A. E. Mallory, *Measurement of meningeal motion using B-mode ultrasound as a step toward understanding the mechanism of subdural hematoma*: The Ohio State University, 2014.

[87] A. Mallory, A. Wetli, L. M. Neuroth, H. Rhule, K. Moorhouse, K. Satterfield, C. Thomas, A. Tesny, and Y.-S. Kang, "Preservatives for postmortem brain tissue in biomechanical testing: A pilot study," *Journal of Anatomy,* vol. n/a, no. n/a, 2024.
[88] S. Budday, T. C. Ovaert, G. A. Holzapfel, P. Steinmann, and E. Kuhl, "Fifty shades of brain: a review on the mechanical testing and modeling of brain tissue," *Archives of Computational Methods in Engineering,* vol. 27, pp. 1187-1230, 2020.
[89] Y. Zhang, T. J. Hughes, and C. L. Bajaj, "An automatic 3D mesh generation method for domains with multiple materials," *Computer methods in applied mechanics and engineering,* vol. 199, no. 5-8, pp. 405-415, 2010.
[90] M. Souli, A. Ouahsine, and L. Lewin, "ALE formulation for fluid–structure interaction problems," *Computer methods in applied mechanics and engineering,* vol. 190, no. 5-7, pp. 659-675, 2000.
[91] N. M. Grosland, K. H. Shivanna, V. A. Magnotta, N. A. Kallemeyn, N. A. DeVries, S. C. Tadepalli, and C. Lisle, "IA-FEMesh: an open-source, interactive, multiblock approach to anatomic finite element model development," *Computer methods and programs in biomedicine,* vol. 94, no. 1, pp. 96-107, 2009.
[92] N. A. Kallemeyn, S. C. Tadepalli, K. H. Shivanna, and N. M. Grosland, "An interactive multiblock approach to meshing the spine," *Computer Methods and Programs in Biomedicine,* vol. 95, no. 3, pp. 227-235, 2009/09/01/, 2009.
[93] A. Schonning, B. Oommen, I. Ionescu, and T. Conway, "Hexahedral mesh development of free-formed geometry: The human femur exemplified," *Computer-Aided Design,* vol. 41, no. 8, pp. 566-572, 2009.
[94] C. Giordano, and S. Kleiven, "Development of a 3-year-old child fe head model, continuously scalable from 1.5-to 6-year-old."
[95] V. S. Alvarez, and S. Kleiven, "Effect of pediatric growth on cervical spine kinematics and deformations in automotive crashes," *Journal of Biomechanics,* vol. 71, pp. 76-83, 2018/04/11/, 2018.

Appendix A. Geometry, material, interface, and element formulation of surface- and voxel-based models

Table A1 - Commonalities in terms of geometric sources, material properties, element formulation, and interfacial conditions in the Conf-model, Vxl-model and Vxls-model

Geometry	***Resource***
Brain/ventricle/subarachnoid CSF/skull	ICBM 152 atlas
Material	***Description***
Brain	Ogden hyperelastic and linear viscoelastic constants: μ_1=53.8 Pa, α_1=10.1, μ_2=-120.4 Pa, α_2=-12.9; G_1=0.31 MPa, G_2=78 kPa, G_3=6.2 kPa, G_4=8.0 kPa, G_5=1.0 kPa, G_6=3.0 kPa; $\beta_1 ... \beta_6 = 10^6 \ldots 10^1$ (1/s), where μ_i and α_i are Ogden parameters, G_i represents the shear relaxation module, and β_i represents the decay constants
Cerebrospinal fluid	Elastic fluid with the bulk modulus as 2.1 GPa
Falx/tentorium/dura mater	Simplified rubber with experimentally derived stress-strain curve
Pia mater	Simplified rubber with experimentally derived stress-strain curve
Skull	Rigid
Element	***Description***
Brain/cerebrospinal fluid/skull	Hexahedral elements with selectively reduced integration
Falx/tentorium/dura mater/pia mater	Quadrilaterals with fully integrated Belytschoko-Tsay membrane
Interface	***Description***
Brain-subarachnoid cerebrospinal fluid interface	Continuous mesh
Subarachnoid cerebrospinal fluid-skull interface	
Brain-ventricle	

Appendix B. Strain of the surface-based model and its counterparts mapped in the image space

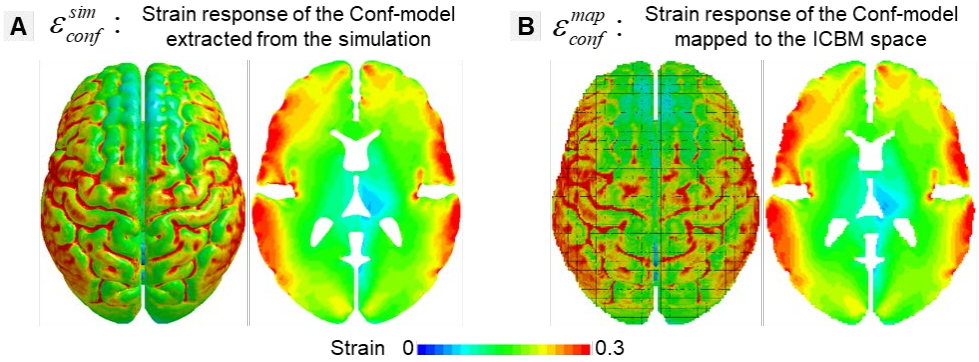

Fig B1. (**A**) Element-wise strain peaks directly simulated by the Conf-model (i.e., ε_{conf}^{sim}). (**B**) Voxel-wise strain peak by mapping strain peaks to the ICBM spaces (i.e., ε_{conf}^{map}). Visually identical strain distribution was noted before and after the mapping, indicating the voxelization procedures captured the strain-related feature of the Conf-model.

Appendix C. Histograms of element number, element size, and mesh quality

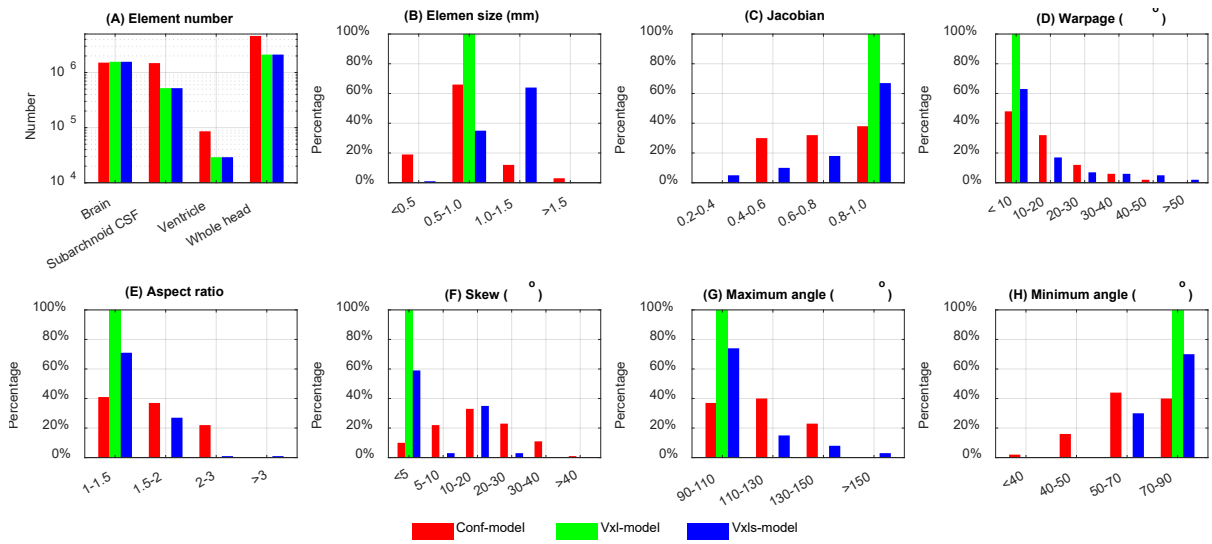

Fig C1. Histograms of element number (A), element size (B), and mesh quality based on 6 indices (C-H) of the Conf-model, Vxl-model, and Vxls-model.